Published in final edited form as:

Neuroimage. 2009 July 15; 46(4): 908–914. doi:10.1016/j.neuroimage.2009.03.019.

Computed tomography of amyloid plaques in a mouse model of Alzheimer's disease using diffraction enhanced imaging

Dean M. Connor[a,*], **Helene Benveniste**[b,c], **F. Avraham Dilmanian**[b,d], **Mary F. Kritzer**[e], **Lisa M. Miller**[a], and **Zhong Zhong**[a]

[a]National Synchrotron Light Source, Brookhaven National Laboratory, Upton, NY 11973, USA

[b]Medical Department, Brookhaven National Laboratory, Upton, NY 11973, USA

[c]Department of Anesthesiology, State University of New York (SUNY), Stony Brook, NY 11794, USA

[d]Department of Radiation Oncology, SUNY, Stony Brook, NY 11794, USA

[e]Department of Neurobiology and Behavior, SUNY, Stony Brook, NY 11794, USA

Abstract

Our understanding of early development in Alzheimer's disease (AD) is clouded by the scale at which the disease progresses; amyloid beta (Aβ) plaques, a hallmark feature of AD, are small (∼50 μm) and low contrast in diagnostic clinical imaging techniques. Diffraction enhanced imaging (DEI), a phase contrast x-ray imaging technique, has greater soft tissue contrast than conventional radiography and generates higher resolution images than magnetic resonance microimaging. Thus, in this proof of principle study, DEI in micro-CT mode was performed on the brains of AD-model mice to determine if DEI can visualize Aβ plaques. Results revealed small nodules in the cortex and hippocampus of the brain. Histology confirmed that the features seen in the DEI images of the brain were Aβ plaques. Several anatomical structures, including hippocampal subregions and white matter tracks, were also observed. Thus, DEI has strong promise in early diagnosis of AD, as well as general studies of the mouse brain.

Introduction

Since Alois Alzheimer's discovery of what is now called Alzheimer's disease (AD), it has been known that plaques in the affected brain are a hallmark of the AD diagnosis. In the mid-1980s, (Glenner and Wong 1984) found that these plaques were composed of clumped together fibrils of amyloid β protein (Aβ), a peptide product of the amyloid precursor protein. Not long afterwards, (Hardy and Higgins 1992) published their amyloid cascade hypothesis, which states that Aβ proteins are the “causative agent of Alzheimer's pathology” and thus an underlying cause of the deleterious effects of AD. If the amyloid hypothesis is correct, then drugs designed to remove the Aβ protein and the associated plaques might cure

*Corresponding author. Fax: +1631 344 3238. address: connord@bnl.gov (D.M. Connor).

Appendix A. Supplementary data: Supplementary data associated with this article can be found, in the online version, at doi:10.1016/j.neuroimage.2009.03.019.

the disease. Thus AD drug development efforts focus on removing the Aβ protein. In order to test the effectiveness of any AD therapy aimed at decreasing the Aβ-plaque load in the brain, it becomes imperative to have a non-invasive, safe, and cost-effective imaging method to track Aβ protein and the number and size of the Aβ plaques within the brain.

Direct tracking of Aβ plaques is a nontrivial task since the individual plaques are both small (5–200 μm) (Esiri et al., 1997) and of low inherent contrast in CT and MRI, and much smaller than the resolution limits of nuclear medicine modalities. Initial efforts of medical imaging research associated with AD have focused on the measurement of gross structural changes that occur in AD, including hippocampal atrophy (Jack et al., 1999). Currently, only MRI, CT, and FDG PET are in routine clinical use for imaging AD patients (DeKosky and Marek, 2003; Petrella et al., 2003), primarily to rule out other possible causes of dementia. Neither modality presently has the combined spatial and contrast resolution necessary to image individual Aβ plaques in the live human brain. Within the last decade, radioligands have been developed to specifically target Aβ within the brain and are used with PET imaging for visualization of the precipitated amyloid plaque load (DeKosky and Marek, 2003; Nichols et al., 2006; Nordberg, 2004; Petrella et al., 2003). These have shown great promise and will likely play a pivotal role in the clinical assessment of AD, assessment of Aβ protein and/or plaque load, and drug efficacy in the future. However, although PET can see the plaques' signature, it cannot provide the spatial resolution to visualize or give the properties of individual Aβ plaques, and thus only provides a measure of the precipitated bulk amount of Aβ in a given brain region.

Several prongs of AD imaging research are underway using MRI. Magnetic resonance spectroscopy (Jessen et al., 2000) provides an indirect measure of the bulk local amyloid load, but cannot visualize or determine properties of individual plaques. Very high field (7 T and greater) research MRI systems have shown the ability to visualize individual plaques in transgenic mice both ex vivo (minimum reported plaque size imaged of about 20 μm) (Benveniste et al., 1999; Braakman et al., 2006; Jack et al., 2004) and in vivo (minimum reported plaque size image of 35 μm) (Braakman et al., 2006; Jack et al., 2005, 2007). MRI visualizes Aβ plaques in the brain tissue because their T2- and T2*-weighted tissue contrast is different than the surrounding tissue (Benveniste et al., 1999). The exact physico-chemical property of the Aβ plaques which causes T2- or T2* contrast changes is at present unknown. It is also important to point out that the T2- or T2* contrast change associated with Aβ plaques is not diagnostic per se because it also occurs in a wide range of other pathological processes (e.g. hemorrhages, inflammation, and ischemia).

Recently, major research efforts have focused on phase contrast x-ray imaging because of its superiority compared to conventional x-ray imaging, especially for soft-tissue imaging applications (Arfelli et al., 1998; Lewis, 2004; Pagot et al., 2005; Wilkins et al., 1996). Propagation-based phase contrast imaging is based on variations in the phase of the transmitted x-ray beam caused by the variations in the electron density in the sample. The resulting contrast is proportional to the second derivative of the phase of the transmitted x-rays. We note that this effect is closely related to the refractive index effect measured by DEI because image contrast in both is related to the real component of the index of refraction, as described below. To date, the only published phase contrast x-ray imaging

study related to AD showed that propagation-based phase contrast imaging is capable of both visualizing individual Aβ plaques and of measuring their mass density ex vivo (Noda-Saita et al., 2006).

Diffraction enhanced imaging (DEI), sometimes referred to as analyzer-based imaging, is a type of phase contrast x-ray imaging in which an analyzer crystal is used to provide image contrast (Chapman et al., 1997). In DEI, a monochromatic synchrotron beam is incident upon a sample. Variations in the real component of the index of refraction within the sample lead to refraction of the transmitted x-ray beam. An analyzer crystal is placed between the sample and the detector. The analyzer crystal has a reflectivity profile, or rocking curve, that has a peak close to unity at the Bragg angle for the particular energy and crystal reflection. Analyzer reflectivity drops to nearly zero within a few microradians. The steep slope of the reflectivity profile converts angular changes in the transmitted beam into intensity changes in the image. DEI has been shown to have significant contrast-to-noise ratio gains over conventional mammography in both planar (Pisano et al., 2000) and CT modes (Fiedler et al., 2004). Furthermore, (Muehleman et al. 2004) have shown that DEI is capable of resolving micron-sized soft tissue structures within cartilage. At present, there are no published studies on the use of DEI to image Aβ plaques.

Because DEI can image soft tissue features at a very high spatial resolution, the hypothesis to be tested here is that DEI, applied in the micro-CT mode (DECT), can both visualize individual Aβ plaques and determine the mass density of each individual plaque in a transgenic mouse brain.

Materials and methods

Specimen preparation

Formalin-fixed brains excised from the skull of a 6-month-old B6C3Tg(APPswe,PSEN1dE9)85Dbo/J transgenic mouse (Jankowsky et al., 2004) (Jackson Laboratory, Bar Harbor, Maine) and an age-matched wild-type mouse were used. The wild-type mouse was a non-carrier mouse from the same colony as the transgenic mouse. Both animals were perfused with PBS and paraformaldehyde prior to fixation. The mouse brains were positioned with minimal external compression in a water-filled acrylic tube (12 mm inner diameter and 1 mm wall thickness) that was placed on top of a rotation stage (D-83253, Huber, Rimsting, Germany). The brain was oriented in the container so that the sagittal plane was parallel to the plane of the x-ray beam.

DECT data acquisition

A diagram of the experimental setup for DEI at the National Synchrotron Light Source (NSLS; Brookhaven National Laboratory, Upton, NY, USA) is shown in Fig. 1 (Zhong et al., 2000). The monochromator and analyzer crystals were aligned to the 20 keV silicon [333] reflection. The height of the x-ray beam was 3 mm and the width was about 36 mm. The digital detector (X-ray Imager VHR 1:1, Photonic Science Limited, UK) has a 36 by 24 mm field of view and a 9 μm pixel size. The rotation stage and sample holder were placed on top of a kinematic mount. Before beginning data acquisition, the detector was leveled

with respect to the incoming x-ray beam and then the rotation stage was leveled with respect to the detector.

In order to obtain the DECT data sets, images were obtained on both the positive and negative sides of the rocking curve. A total of 2000 images were acquired at both the +1.2 and −1.2 μ radian points on the reflectivity profile (roughly the half reflectivity points), in addition 50 dark images and 100 air images were acquired for each of the analyzer crystal positions. The images were taken in 0.18° increments over 360°. The acquisition time was 1 s per projection image. The dark images were acquired with the shutter closed, thus with no incident beam on the detector. The air images were acquired by lowering the sample out of the beam and imaging only the air. The average total absorbed dose within the brain was 28 Gy. The brain height was greater than that of the beam, thus the rotation stage was raised in 2.8 mm increments after acquisition of each of CT projections until the full brain was imaged.

Image reconstruction

After air and background corrections, the data from the opposite sides of the reflectivity profile were then combined according to Chapman's DEI refraction equation (Chapman et al., 1997):

$$\Delta\theta_z = \frac{I_H R(\theta_L) - I_L R(\theta_H)}{I_L \left(\frac{dR}{d\theta}\right)(\theta_H) - I_H \left(\frac{dR}{d\theta}\right)(\theta_L)} \quad (1)$$

where $\Delta\theta_z$ is the total up-down angular deviation of the beam, I_H and I_L are the measured intensity on the positive and negative side of the reflectivity profile, respectively, and R is the reflectivity of the analyzer crystal as a function of the detuning angle θ (that is the deviation from the Bragg peak). The planar refraction images then served as the projection images for the refraction DECT image reconstruction (Dilmanian et al., 2000). Images were reconstructed using filtered backprojection. The reconstructed image sets were combined to form a volumetric data set of the brain. The volumetric data set represents a map of the *z*-gradient of the index of refraction. From this volumetric data, planar images were generated along the vertical plane, perpendicular to the plane of the x-ray beam, thereby generating coronal sections of the brains. For each image, each set of seven adjacent coronal slices were averaged together; thus the resulting voxels had an in-plane size of 9 by 9 μm and an out-of-plane size of 63 μm.

Immunocytochemistry

Brains were blocked posterior to the hypothalamus, the left hemispheres were marked with subcortically placed artifacts, and the tissue was coronally sectioned on a freezing microtome (40 μm). Separate rostrocaudal series of sections from each animal were then immunoreacted using a monoclonal antibody recognizing the mouse beta amyloid protein (the generous gift from Dr. William Van Nostrand, Department of Infectious Diseases, Stony Brook University). In preparation, endogenous peroxidase was eliminated by incubating the sections in 1% H_2O_2 (45 min). Afterward, the sections rinsed repeatedly in 50

mM Tris buffered saline (TBS), pH 7.4. Next, the sections were placed in a blocking solution (50 mM TBS containing 10% normal swine serum—NSS) for 2 h, prior to incubation in anti-beta amyloid antibody (2–3 days, diluted 1:500 in TBS containing 1% NSS, 4 °C). The tissue sections were then rinsed in TBS, incubated in biotinylated secondary antibodies (Vector, Burlingame, CA., 2 h, room temperature, working dilution 1:100), additionally rinsed in TBS, and then were placed in avidin–biotin-complexed horseradish peroxidase (ABC, Vector, 2 h, room temperature). After this step, sections were rinsed in Tris buffer, pH 7.6, and reacted using 0.07% 3,3′-diaminobenzidine (DAB, brown reaction product) as chromagen. As a control, immunocytochemical labeling was carried out on representative sections with the omission of primary antisera. Brightfield, low power histology images were obtained using a Zeiss Stemi 2000 dissecting scope interfaced with a Zeiss Axiocam (B/W digital camera) and Axiovision acquisition software; the magnification is 8×; the digital image was converted to a Tiff file and adjusted for contrast and brightness only.

Determining plaque size, number density, and physical density

From the coronal slice refraction DECT images the plaque sizes, contrast-to-noise ratio, and density were measured for different plaques (n = 100). The plaque sizes were determined using a line profile through a plaque by measuring the distance between the peak (upward refraction) and trough (downward refraction) of the refraction signal. The contrast-to-noise ratio was found according to Eq. [2],

$$\mathrm{CNR}=\frac{\left(\frac{\partial n}{\partial z}\right)_{\max}-\left(\frac{\partial n}{\partial z}\right)_{\min}}{\sigma} \quad (2)$$

where $\partial n/\partial z_{\max,\min}$ are the maximum and minimum values of z-gradient of the index of refraction through the plaque and σ is the standard deviation of a feature-free region of the image.

The number density of the plaques was measured in the cortex region of the brain. To do this, a DECT slice image was opened in the NIH Image program (developed at the U.S. National Institutes of Health and available on the Internet at http://rsb.info.nih.gov/nih-image/). The freehand selection tool was used to outline the cortex and measure the cortex size. Within the image, each of the plaques was marked and counted. In order to ensure that only plaques were counted, and not blood vessels, the DECT slice image was compared to adjacent slice images; if the feature seen in the slice image was a blood vessel, then it will be apparent upon looking at the adjacent slices since blood vessels are tube-like structures whereas plaques are more spherical. The plaque density was then calculated according to Eq. [3],

$$\rho=\frac{n}{At} \quad (3)$$

where ρ is the number density of the plaques in the cortex, n is the number of plaques counted, A is the cortex area in the slice, and t is the slice thickness. This procedure was

repeated for five additional slices. The mean and the standard deviation of the number density of the plaques were determined.

To determine the mass density of the plaques relative to the surrounding brain tissue, first the refraction signal from an interface between two materials of known density (air and water) was found. This was done through measuring the $\partial n/\partial z$ maxima and minima on a line profile through an air bubble of similar size to the plaques. Since $\Delta\rho$ at the water–air bubble interface is known (1 g/cm^3) and because $\Delta\rho$ is proportional to Δn, $\Delta\rho$ of the brain–plaque interface, and thus the mass density of the plaques, can be determined through measuring the refraction amount relative to the refraction amount at the air–water interface. Plaques from the cortex region from four slices were analyzed and the mean and standard deviation of $\Delta\rho$ were determined.

Results

AD-model and wild-type comparison

The volumetric refraction DECT data from the AD-model mouse brain were compared to the DECT data for a wild-type mouse brain. Such a comparison for coronal slice images is presented in Fig. 2. Both images show a detailed view of the anatomical structure. Fig. 2a includes labeling of the anatomical structures in the wild-type brain. In addition to revealing ventricular spaces, the contrast that is achieved between regions of gray and white matter enables a clear delineation of fiber tracts, including the large corpus callosum, fasciculus retroflexus and cerebral peduncles. These, as well as smaller tracts and white matter-enriched laminae that are also visible, create outlines that enable identification of discrete gray matter structures. The cerebral cortex, the cornu ammonis (CA) fields of the hippocampus, the dentate gyrus, and several individual nuclei of the thalamus can be seen (surrounded by the external medullary lamina and the medial lemniscus of the thalamus). Supplemental Figs. 1 and 2 present refraction DECT videos of coronal sections through the full wild-type and AD-model mouse brains, respectively.

In the AD-model brain, small nodules can be seen throughout the cerebral cortical mantle and within the hippocampus. The DEI contrast of the nodules is white over black meaning that the nodules are denser than the surrounding tissue. These nodules occupy regions where Aβ plaques are typically concentrated and are not visible in the WT mouse brain. Figs. 2b and e show the zoomed-in views of corresponding regions of the cortex of the WT and AD-model mouse brains. The WT brain is noticeably smoother than the AD-model brain. The same is true for Fig. 2c and f that display a zoomed-in view of the hippocampus region of the two brain types.

Comparison of AD-model to histology

After imaging was completed, the AD-model mouse brain was sectioned and immunostained for comparison with the DECT data. Fig. 3 shows the image of an immunostained histology coronal section from the AD-model mouse brain along with its corresponding DECT slice image. Plaques can be clearly seen throughout the cortex and hippocampus regions of the histology image, just as the nodules can be seen in the DECT

image. The zoomed-in images of the histology and DECT image are displayed in Figs. 3b and d. Within the zoomed-in region, there is a near one-to-one correspondence between the nodules in the DECT image and the plaques in the histology image (as pointed out by the arrows in Figs. 3b and d). Because of the steps involved in generating an immunostained histology slice, it is not feasible to generate a slice image that fully corresponds between histology and DECT; the freezing, slicing and staining processes lead to distortions and warping of the brain, making it impossible to generate fully corresponding images. Thus, it is only feasible to have correspondence over small regions of the images. The usefulness of image comparison lies both in large-scale correspondence or global values of plaque locations, sizes, and number densities, and in small-scale correspondence over a small image region.

From the histology, the plaques averaged 52±18 μm (mean± standard deviation) in diameter. From the DECT images, the plaques averaged 44±13 μm in diameter. The difference can be explained as follows. Plaques have a dense core consisting primarily of the Aβ protein and a loosely packed external region Aβ and other associated proteins (Noda-Saita et al., 2006). Since DEI is sensitive to changes in local density, it is expected that it would be less sensitive to the loosely packed external region and more sensitive to the denser central region. Thus, one would expect the average plaque size as measured by DEI to be smaller than that measured through histology.

From histology, the number density of the plaques (defined as the number of plaques per unit volume) in the cortex was 87 plaques/mm^3 in the displayed slice. The corresponding cortex plaque number density from the displayed DECT slice image was 80 plaques/mm^3. There was some variation in the number density of plaques in the cortex region from slice to slice in the DECT slices. For example the plaque density in five randomly selected DECT slice images, averaged 69±8 plaques/mm^3 with a range from 58 to 80 plaques/mm^3. Because of the substantial variation in the number density of plaques in the cortex region as measured from several different DECT refraction slice images, and because it was not possible to fully align the slice image from the 3D DECT refraction data to the histological slice image, it is fair to say that the number density of plaques as measured with DECT agrees with the measured number density as measured from histology. The plaques seen in the histology image are primarily neuritic, dense core plaques. Because the plaque counts in histology and DECT are similar, DECT is visualizing neuritic, dense core plaques.

Properties of plaques from refraction DECT

Averaging over five DECT slice images, the cortical plaque number density was 69 ±8 plaques/mm^3, and thus the Aβ plaques take up 0.29 ± 0.04% of the brain's cortical volume. The contrast-to-noise ratio (CNR) of the plaques was 9±2 and ranged from 5 to 12. The relative difference in physical density (defined as the mass per unit volume) between the plaques and the surrounding brain tissue, $\Delta\rho$ was measured to be + 21 ± 4 mg/cm^3 and ranged in $\Delta\rho$ from +13 to + 31 mg/cm^3. It is unlikely that iron concentration in the plaque substantially contributes to the contrast. In order for a feature to be visible with DECT, it must have a measurable difference in density from the surrounding material. Iron content within plaques is responsible for a density increase of 0.006% within the plaque (relative to

the surrounding tissue) (Lovell et al., 1998), which is far below the observed 2% density difference recorded here.

Discussion

Our primary finding in this technology-driven, proof of principle study is that DECT-based x-ray imaging can be used, without histological sectioning, to visualize a wide range of anatomical substructures within the mouse's brain without the use of a contrast agent. Specifically we show that, in a whole mouse brain, and without the use of contrast agents, DECT resolves Aβ plaques below 30 μm in diameter that vary in density by ∼2% from the surrounding brain tissue. This is an important and promising result because it is well accepted that all x-ray approaches (e.g. micro-CT) are incapable of visualizing anatomical structures within the rodent brain without the use of contrast agents.

Because of DECT's ability to generate soft tissue contrast, the images are more similar in appearance to high resolution magnetic resonance imaging (referred to as magnetic resonance microscopy or MRM) (Benveniste et al., 2000) than to standard micro-CT. Supplemental Fig. 3 presents coronal section video comparison between the refraction DECT of the wild-type mouse brain and in vitro, high field (17.6 T) MRM T2* images from the 3-D MRI digital atlas database of an adult C57BL/6J mouse brain (Ma et al., 2005, 2008). MRM has been used to create rodent brain atlases in vivo (Bock et al., 2006) and in vitro (Ma et al., 2005) because of its excellent tissue contrast and its spatial resolution (in the range of 20–40 μm^3). The MRM brain atlases can therefore be used to define and display substructures in all dimensions and used to quantify, map, and display a variety of data (Ma et al., 2005). Our work presented here shows that DECT also has the potential to display mouse brain anatomy with high anatomical accuracy. For example, on the DECT images we were able to easily identify at least ten different brain regions at the level of the ventral hippocampus alone. Considering that DEI has a theoretical maximum resolution of about 2 μm, it is possible that DEI can be used to create rodent brain atlases with higher spatial resolution compared to atlases created by MRM.

DEI has unique and unexplored image contrast for brain tissue. We are planning to further explore this potential of DEI in studies focused on visualizing mouse brain anatomy in normal and transgenic mouse models of AD in vivo using DEI. This is a complicated task because the subtle contrast of the plaques is obfuscated by CT artifacts generated at the skull–brain interface. Because the skull causes the attenuation, extinction, and refraction of x-rays, and all to a much greater extent than the surrounding tissue, reconstruction artifacts are generated by the skull. DEI has two major advantages over propagation-based phase contrast for achieving the goal of imaging through the skull. First, for a given energy, DEI has greater contrast than propagation-based imaging (Pagot et al., 2005). Second, DEI's contrast is inversely proportional to the x-ray energy (Chapman et al., 1997; Zhong et al., 2000), whereas propagation-based phase contrast has inverse squared relationship with energy (Pagot et al., 2005). Thus, it is possible to use higher energy x-rays in order to reduce attenuation from the skull, while still being able to resolve individual plaques. Initial studies have shown that the hippocampus/cortex interface can be visualized with DECT when

imaging through the skull (Connor et al., 2007), but in vivo studies with living transgenic mice have yet to be performed.

For this study, the limiting factor for minimum resolvable plaque size was the detector, which has a pixel size of 9 μm. DECT has a theoretical lower limit for resolution of around 2 μm, thus DECT should be able to resolve even the smallest neuritic plaques (5 μm). Further future studies will focus on high contrast and high resolution (<5 μm) DECT of whole, excised brains. This technique has the advantage of requiring minimal processing of the brain prior to imaging; several of the intervening steps required for histological sectioning can be removed.

The resolution, and thus high dose, required for imaging individual plaques makes it unlikely that DECT can be used for resolving individual, developing plaques in vivo in humans. Lower dose planar DEI can yielda measure of relative plaque load. When DEI is performed with the analyzer on the peak of the rocking curve, the net angular deviation of the beam by the plaques leads to a reduction of x-ray intensity (extinction contrast); this gives a macroscopic measurement of the average Aβ plaque load within the brain. In future studies, we will measure the extinction contrast as a function of Aβ plaque load.

Supplementary Material

Refer to Web version on PubMed Central for supplementary material.

Acknowledgments

The authors would like to thank Dr. William Van Nostrand for his contribution to this study. Use of the X15A beamline at the NSLS, BNL, was supported by the U.S. Department of Energy, Office of Basic Energy Sciences, under contract number DE-AC02-98CH10886, the Brookhaven National Laboratory LDRD 05-057, NIH grant R01 AR48292, and NIH/NCI grant CA111976.

References

Arfelli F, Assante M, Bonvicini V, Bravin A, Cantatore G, Castelli E, Dalla Palma L, Di Michiel M, Longo R, Olivo A, Pani S, Pontoni D, Poropat P, Prest M, Rashevsky A, Tromba G, Vacchi A, Vallazza E, Zanconati F. Low-dose phase contrast x-ray medical imaging. Phys Med Biol. 1998; 43:2845–2852. [PubMed: 9814522]

Benveniste H, Einstein G, Kim KR, Hulette C, Johnson GA. Detection of neuritic plaques in Alzheimer's disease by magnetic resonance microscopy. Proc Natl Acad Sci. 1999; 96:14079–14084. [PubMed: 10570201]

Benveniste H, Kim K, Zhang L, Johnson GA. Magnetic resonance microscopy of the C57BL mouse brain. Neuroimage. 2000; 11:601–611. [PubMed: 10860789]

Bock NA, Kovacevic N, Lipina TV, Roder JC, Ackerman SL, Henkelman RM. In vivo magnetic resonance imaging and semiautomated image analysis extend the brain phenotype for cdf/cdf mice. J Neurosci. 2006; 26:4455–4459. [PubMed: 16641223]

Braakman N, Matysik J, van Duinen SG, Verbeek F, Schliebs R, de Groot HJM, Alia A. Longitudinal assessment of Alzheimer's β-amyloid plaque development in transgenic mice monitored by in vivo magnetic resonance microimaging. J Magn Reson Imaging. 2006; 24:530–536. [PubMed: 16892201]

Chapman D, Thomlinson W, Johnston RE, Washburn D, Pisano E, Gmur N, Zhong Z, Menk R, Arfelli F, Sayers D. Diffraction enhanced x-ray imaging. Phys Med Biol. 1997; 42:2015–2025. [PubMed: 9394394]

Connor, D.; Dilmanian, FA.; Parham, C.; Kao, T.; Zhong, Z. Energy and dose considerations for diffraction enhanced CT in small animal studies. In: Hsieh, J.; Flynn, MJ., editors. Medical Imaging 2007: Physics of Medical Imaging. SPIE; Bellingham, WA: 2007. p. 65103K-65101.p. 65109

DeKosky ST, Marek K. Looking backward to move forward: early detection of neurodegenerative disorders. Science. 2003; 302:830–834. [PubMed: 14593169]

Dilmanian FA, Zhong Z, Ren B, Wu XY, Chapman LD, Orion I, Thomlinson WC. Computed tomography of x-ray index of refraction using the diffraction enhanced imaging method. Phys Med Biol. 2000; 45:933–946. [PubMed: 10795982]

Esiri, MM.; Hyman, BT.; Beyreuther, K.; Masters, CL. Greenfield's Neuropathology. 6th. Graham, DI.; Lantos, PL., editors. Arnold; London: 1997. p. 153-234.

Fiedler S, Bravin A, Keyrilainen J, Fernandez M, Suortti P, Thomlinson W, Tenhunen M, Virkkunen P, Karjalainen-Lindsberg ML. Imaging lobular breast carcinoma: comparison of synchrotron radiation DEI-CT technique with clinical CT, mammography and histology. Phys Med Biol. 2004; 49:175–188. [PubMed: 15083665]

Glenner GC, Wong CW. Alzheimer's disease: initial report of the purification and characterization of a novel cerebrovascular amyloid protein. Biochem Biophys Res Commun. 1984; 20:885–890. [PubMed: 6375662]

Hardy JA, Higgins GA. Alzheimer's disease: the amyloid cascade hypothesis. Science. 1992; 256:184–185. [PubMed: 1566067]

Jack CR, Petersen RC, Xu YC, O'Brien PC, Smith GE, Ivnik RJ, Boeve BF, Waring SC, Tangalos EG, Kokmen E. Prediction of AD with MRI-based hippocampal volume in mild cognitive impairment. Neurology. 1999; 52:1397–1403. [PubMed: 10227624]

Jack CR Jr, Garwood M, Wengenack TM, Borowski BJ, Curran GL, Lin J, Adriany G, Grohn OHJ, Grimm R, Poduslo JF. In vivo visualization of Alzheimer's amyloid plaques by magnetic resonance imaging in transgenic mice without a contrast agent. Magn Reson Med. 2004; 52:1263–1271. [PubMed: 15562496]

Jack CR Jr, Wengenack TM, Reyes DA, Garwood M, Curran GL, Borowski BJ, Lin J, Preboske GM, Holasek SS, Adriany G, Poduslo JF. *In vivo* magnetic resonance microimaging of individual amyloid plaques in Alzheimer's transgenic mice. J Neurosci. 2005; 25:10041–10048. [PubMed: 16251453]

Jack CR Jr, Marjanska M, Wengenack TM, Reyes DA, Curran GL, Lin J, Preboske GM, Poduslo JF, Garwood M. Magnetic resonance imaging of Alzheimer's pathology in the brains of living transgenic mice: a new tool in Alzheimer's disease research. Neurosci. 2007; 13:38–48.

Jankowsky J, Fadale D, Anderson J, Xu G, Gonzales V, Jenkins N, Copeland N, Lee M, Younkin L, Wagner S, Younkin S, Borchelt D. Mutant presenilins specifically elevate the levels of the 42 residue beta-amyloid peptide in vivo: evidence for augmentation of a 42-specific gamma secretase. Hum Mol Genet. 2004; 13:159–170. [PubMed: 14645205]

Jessen F, Block W, Traber F, Keller E, Flacke S, Papassotiropoulos A, Lamerichs R, Heun R, Schild HH. Proton MR spectroscopy detects a relative decrease of N-acetylaspartate in the medial temporal lobe of patients with AD. Neurology. 2000; 55:684–688. [PubMed: 10980734]

Lewis RA. Medical phase contrast x-ray imaging: current status and future prospects. Phys Med Biol. 2004; 49:3573–3583. [PubMed: 15446788]

Lovell MA, Robertson JD, Teesdale WJ, Campbell JL, Markesbery WR. Copper, iron and zinc in Alzheimer's disease senile plaques. J Neurol Sci. 1998; 158:47–52. [PubMed: 9667777]

Ma Y, Hof PR, Grant SC, Blackband SJ, Bennett R, Slatest L, McGuigan MD, Benveniste H. A three-dimensional digital atlas database of the adult C57BL/6J mouse brain by magnetic resonance microscopy. Neuroscience. 2005; 135:1203–1215. [PubMed: 16165303]

Ma Y, Smith D, Hof P, Foerster B, Hamilton S, Blackband S, Yu M, Benveniste H. In vivo 3D digital atlas database of the adult C57BL/6J mouse brain by magnetic resonance microscopy. Front Neuroanat. 2008; 2

Muehleman C, Majumdar S, Issever AS, Arfelli F, Menk RH, Rigon L, Heitner G, Reime B, Metge J, Wagner A, Kuettner KE, Mollenhauer J. X-ray detection of structural orientation in human articular cartilage. Osteoarthr Cartil. 2004; 12:97–105. [PubMed: 14723869]

Nichols L, Pike VW, Cai L, Innis RB. Imaging and in vivo quantitation of β-amyloid: an exemplary biomarker for Alzheimer's disease? Biol Psychiatry. 2006; 59:940–947. [PubMed: 16487944]

Noda-Saita K, Yoneyama A, Shitaka Y, Hirai Y, Terai K, Wu J, Takeda T, Hyodo K, Osakabe N, Yamaguchi T, Okada M. Quantitative analysis of amyloid plaques in a mouse model of Alzheimer's disease by phase-contrast X-ray computed tomography. Neuroscience. 2006; 138:1205–1213. [PubMed: 16460878]

Nordberg A. PET imaging of amyloid in Alzheimer's disease. Lancet Neurol. 2004; 3:519–527. [PubMed: 15324720]

Pagot E, Fiedler S, Cloetens P, Bravin A, Coan P, Fezzaa K, Baruchel J, Hartwig J. Quantitative comparison between two phase contrast techniques: diffraction enhanced imaging and phase propagation imaging. Phys Med Biol. 2005; 50:709–724. [PubMed: 15773629]

Petrella JR, Coleman RE, Doraiswamy PM. Neuroimaging and early diagnosis of Alzheimer disease: a look to the future. Radiology. 2003; 226:315–336. [PubMed: 12563122]

Pisano ED, Johnston RE, Chapman D, Geradts J, Iacocca MV, Livasy CA, Washburn DB, Sayers DE, Zhong Z, Kiss MZ, Thomlinson WC. Human breast cancer specimens: diffraction-enhanced imaging with histologic correlation — improved conspicuity of lesion detail compared with digital radiography. Radiology. 2000; 214:895–901. [PubMed: 10715065]

Wilkins SW, Gureyev TE, Gao D, Pogany A, Stevenson AW. Phase-contrast imaging using polychromatic hard x-rays. Nature. 1996; 384:335–338.

Zhong Z, Thomlinson W, Chapman D, Sayers D. Implementation of diffraction-enhanced imaging experiments: at the NSLS and APS. Nucl Instrum Methods Phys Res A. 2000; 450:556–567.

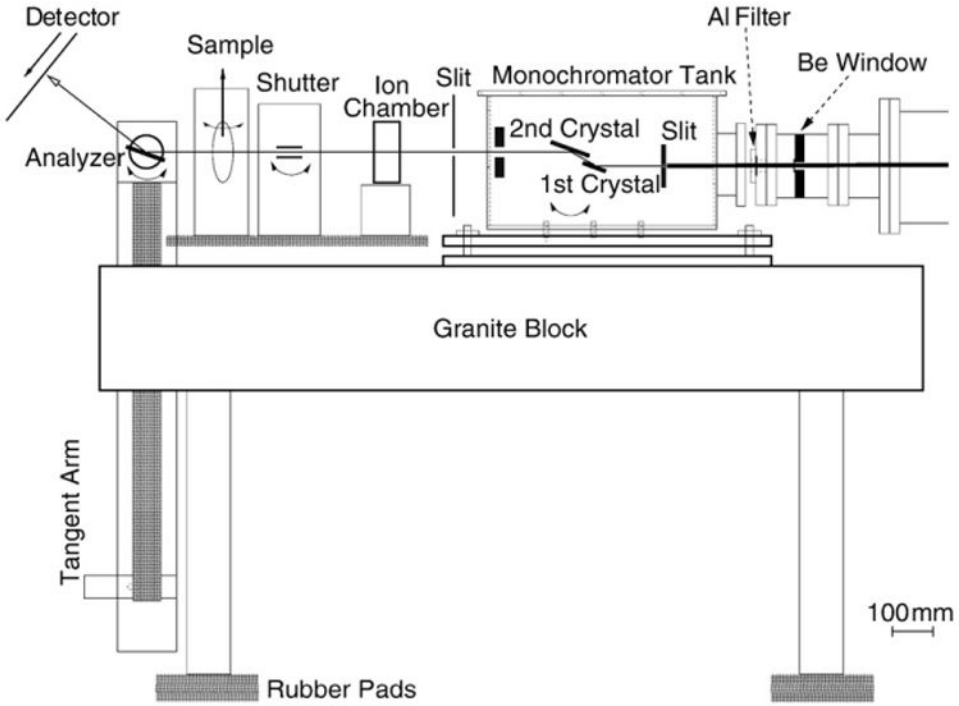

Fig. 1.
Diagram of the DEI experimental setup at beamline X15A at the NSLS.

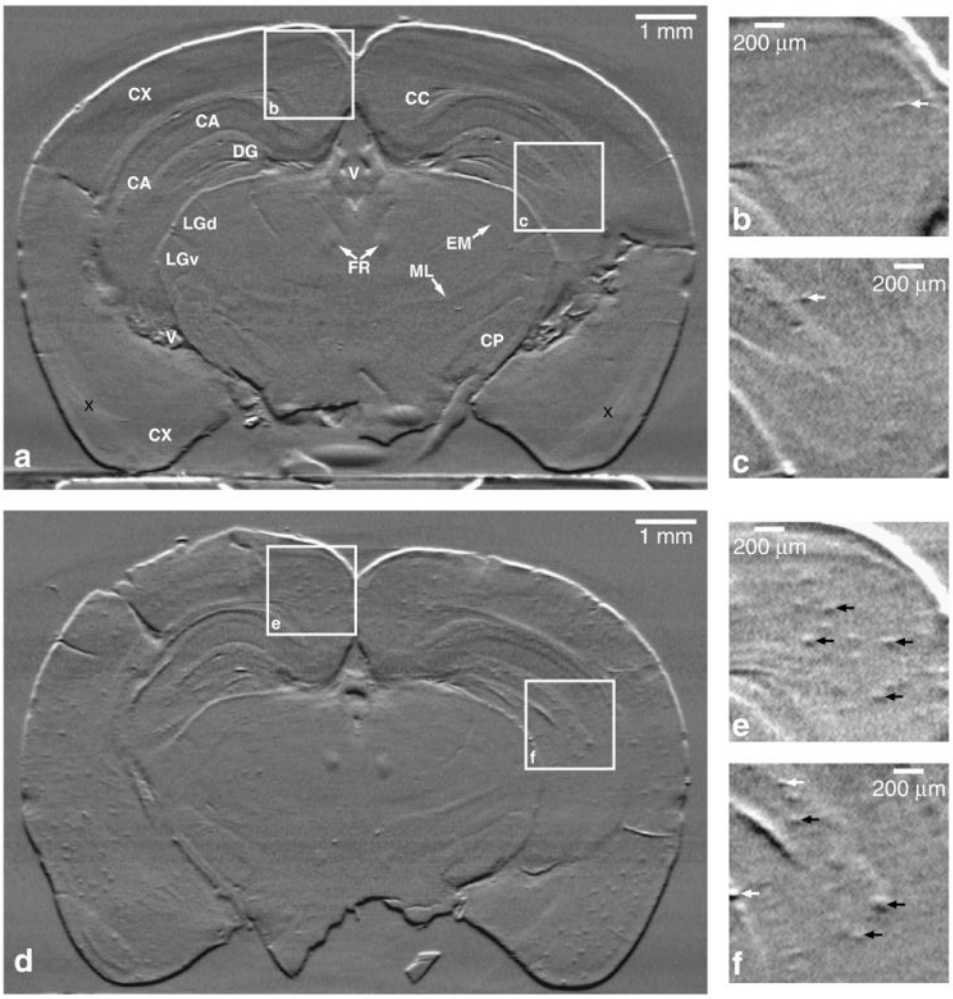

Fig. 2.

Comparison between DECT slice images of the wild-type (a) and transgenic mouse (d) both taken with an in-plane size of 9 by 9 µm and an out-of-plane size of 63 µm. Several anatomical features are labeled in the wild-type brain including the cortex (**CX**), the CA fields in the hippocampus (**CA**), the corpus collosum (**CC**), the dentate gyrus (**DG**), the external medullary lamina of the thalamus (**EM**), the dorsal and ventral parts of the lateral geniculate nuclei of the thalamus (**LGd, LGv**), the fasciculus retroflexus (**FR**), the medial lemniscus (**ML**), the cerebral peduncles (**CP**) and ventricular spaces (**V**). The black **x**'s demark image artifacts. Images (b) and (c) are zoomed-in views from the wild-type brain; images (e) and (f) are zoomed-in views of the corresponding region of the transgenic mouse brain. White arrows are used to demark blood vessels, while black arrows are used to demark nodules.

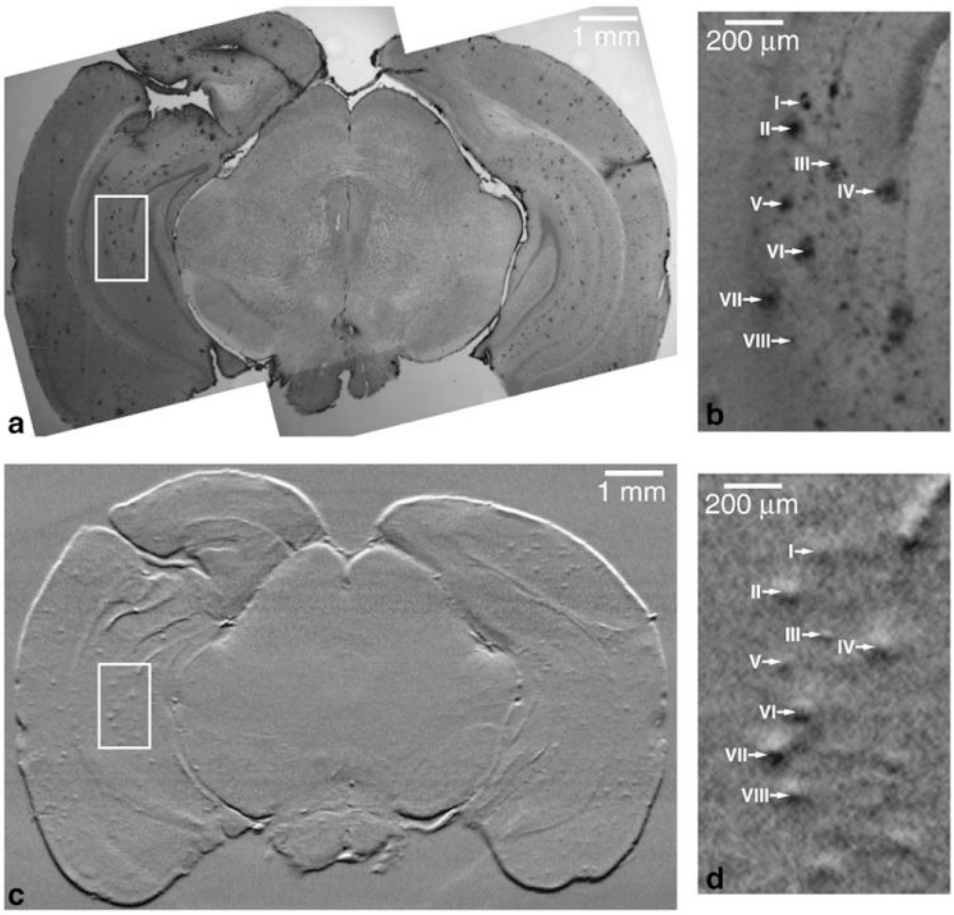

Fig. 3.

Slice images of the brain of a transgenic mouse obtained through histology (a) and the corresponding brain region imaged with DECT (c). Zoomed-in views of the boxed regions of (a) and (c) are presented in (b) and (d), respectively. The numbered arrows point to plaques [in (b)] and nodules [in (d)].